

Propeller Performance Data at Low Reynolds Numbers

John B. Brandt* and Michael S. Selig[†]

University of Illinois at Urbana-Champaign, Urbana, IL 61801, USA

While much research has been carried out on propellers for full-scale aircraft, not much data exists on propellers applicable to the ever growing number of UAVs. Many of these UAVs use propellers that must operate in the low Reynolds number range of 50,000 to 100,000 based on the propeller chord at the 75% propeller-blade station. Tests were performed at the University of Illinois at Urbana-Champaign (UIUC) to quantify the propeller efficiency at these conditions. In total, 79 propellers were tested and the majority fit in the 9- to 11-in diameter range. During the tests, the propeller speed (RPM) was fixed while changing the wind-tunnel speed to sweep over a range of advance ratios until reaching the windmill state (zero thrust). To examine Reynolds number effects, typically four RPM's were tested in the range 1,500 to 7,500 RPM depending on the propeller diameter. Propeller efficiencies varied greatly from a peak near 0.65 (for an efficient propeller) to near 0.28 (for an exceptionally poor propeller). Thus, these results indicate that proper propeller selection for UAVs can have a dramatic effect on aircraft performance.

I. Introduction

Propeller performance at low Reynolds numbers has become increasingly important in the design and performance prediction of unmanned air vehicles (UAVs). While propeller performance for full-scale airplanes has been well documented since the pioneering days of aviation, data on propellers at low Reynolds numbers has been scarce. Tests performed by Bailey¹ documented tests on seven wooden Top Flite™ model-airplane propellers ranging in diameter from 9 to 14 in. It was reported that those results showed propeller efficiencies 7.5% to 15% lower than larger 36-in diameter propellers having similar pitch-to-diameter ratios tested by Durand.² Similar degradation in performance was later measured by Bass³ for propellers larger than 24-in diameter and also by Asson and Dunn⁴ showing data on two wooden 14-in diameter Zinger brand model airplane propellers. During the same time period that current tests were performed,⁵ Merchant and Miller conducted tests on as many as 30 model airplane propellers ranging in diameter from 6 to 22 in, but only a subset of the measurements on seven propellers have been reported from that effort.^{6,7} More recently Ol, et al.⁸ carried out measurements on many propellers aimed toward use on UAVs and made detailed comparisons with analysis, revealing important low Reynolds number effects. These recent measurements on small-scale propellers and the results reported here have all been motivated by the same interests in documenting the aerodynamic performance of small-scale propellers that are used in small UAVs and other low Reynolds number applications.

In the research reported here, 79 propellers were tested and nearly all fit in the 9- to 11-in diameter range. Thrust and torque were measured over a range of propeller advance ratios for discrete propeller speeds (RPM's) – typically four different values of RPM to examine low Reynolds number effects. Also static thrust was measured over a range of propeller speeds from nominally 1500 to 7500 RPM depending on the propeller diameter.

The remainder of this paper describes the propellers tested, the experimental setup, and presents some of the measurements obtained, including some discussion of Reynolds number effects observed in the data.

*Currently with Boeing, Aerodynamics - Stability & Control, Seattle, WA. Member AIAA.

[†]Associate Professor, Department of Aerospace Engineering, 104 S. Wright St. Senior Member AIAA.
<http://www.ae.illinois.edu/m-selig>



Figure 1. Photograph of test section with experimental rig installed.

The entire dataset is available online.⁹

II. Experimental Setup

A. UIUC Wind Tunnel

The tests presented here were performed in the UIUC subsonic wind tunnel. The wind tunnel is an open-return type with a 7.5:1 contraction ratio. The rectangular test section is nominally 2.8×4.0 ft (0.853×1.219 m) in cross section and 8-ft (2.438-m) long. Over the length of the test section, the width increases by approximately 0.5 in. (1.27 cm) to account for boundary-layer growth along the tunnel sidewalls. Test-section speeds are variable up to 160 mph (71.53 m/sec) via a 125-hp (93.25-kW) AC motor connected to a five-bladed fan. For the tests presented here, the maximum tunnel speed used was 80 ft/sec (24.38 m/sec). A photograph of the test section is presented in Fig. 1.

In order to ensure good flow quality in the test section, the wind-tunnel settling chamber contains a 4-in. thick honeycomb in addition to four anti-turbulence screens. The turbulence intensity has been measured to be less than 0.1% for the empty tunnel,¹⁰ showing that the tunnel indeed has good flow quality. The turbulence intensity for varying wind tunnel speeds was measured with hotwire anemometry. After calibrating the hotwire, the probe was placed at the centerline of the tunnel and oriented to measure the axial turbulence intensity. In order to monitor the turbulence intensity over a broad range of frequencies, 50,000 samples were acquired at 10,000 Hz. Figure 2 shows the turbulence intensities for the approximate range of velocities used in the present experiment with various high-pass filters applied to the signal. Assuming that the test apparatus has a minimal effect on the turbulence levels, the good flow quality will be retained.

B. Thrust and Torque Measurements

The test apparatus is pictured in Fig. 3. The thrust and torque produced by a right-handed propeller are illustrated. The thrust measurement was obtained outside the wind tunnel through a pendulum T-shaped structure that pivoted about two flexural pivots while being constrained by a load cell outside of the tunnel. The Interface model SM-10 load cell was used, having a maximum capacity of 10 lbs. To ensure that the freestream flow did not produce a drag force on the beam located inside of the tunnel, a fairing was used as shown in Fig. 1.

To minimize measurement uncertainty in thrust, flexural pivots and a variable load-cell location were used. The flexural pivots, made by Goodrich Aerospace, are frictionless, stiction-free bearings with negligible hysteresis that are designed for applications with limited angular travel (± 30 deg). The pivots are made with flat, crossed springs (that visually appear like a crosshair) that support rotating sleeves. These flexural pivots were chosen over standard bearings because they greatly reduce the adverse tendencies that bearings

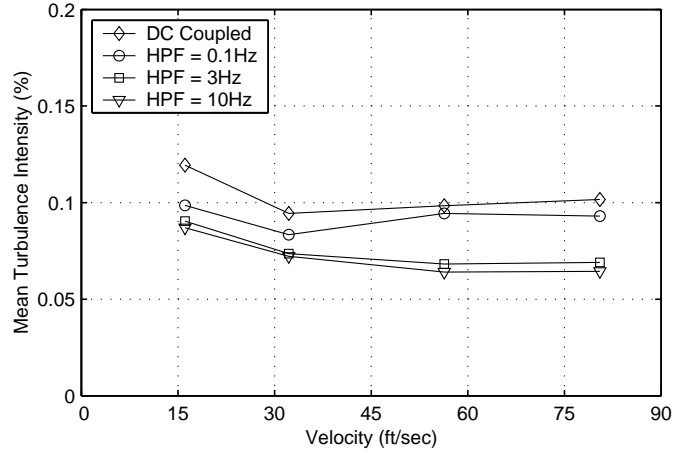


Figure 2. Turbulence intensity at tunnel centerline.

are prone to when used in static applications, namely stiction and hysteresis. The test rig was designed to use the 3/8 in. double-ended series (part number 6012-600). The upper balance arm of the mechanism was designed to allow the load cell to be placed any of 10 possible locations, which allowed the balance arm to be varied from 3.75 in. (9.53 cm) to 12.75 in. (32.39 cm), in 1 in. (2.54 cm) increments. This feature ensured that the load cell could be placed in a position such that the full range of the load cell was used for each propeller tested.

The torque produced by the propeller was measured using the RTS-25 and RTS-100 reaction torque transducers made by Transducer Techniques. These devices are simply force transducers housed and calibrated so that, when placed appropriately, a torque can be measured. The rig was designed with the torque transducer placed between the motor housing and support arm of the thrust mechanism, as is shown in Fig. 4. One of two torque transducers (25 oz-in. or 100 oz-in. capacities) was used depending on the expected maximum torque.

C. Propeller Speed Measurement

To measure the propeller rotation speed, a photoreflector was used to count the number of revolutions the output shaft made in a fixed time interval (0.75 sec). The photoreflector was a Honeywell HOA1180-002 Reflective Sensor, which has a transistor output and allows the sensor to be placed up to 0.5 in. (1.27 cm) from the reflective surface. When combined with a simple circuit of resistors and a 9-V battery, the output voltage was near 2 V when aimed at a reflective surface and near 0 V when aimed at a non-reflective surface. The circuit had a response time around 5 μ sec. The output voltages and response time of the circuit proved to be more than sufficient for measuring the rotational speed of the propellers, which never exceeded 7,000 RPM in these tests.

D. Freestream Flow Speed Measurement

The freestream flow speed was measured with a pitot-tube connected to a differential pressure transducer, an absolute differential pressure transducer, and a thermocouple. The dynamic pressure is measured with the pitot tube connected to one of two MKS differential pressure transducers – a MKS model 220DD 1-torr transducer used when the velocity is below 40 ft/sec and a MKS model 221BD 10-torr model used when the velocity exceeds 40 ft/sec. The atmospheric pressure outside of the tunnel is measured with an MKS absolute pressure transducer. The temperature is measured with an Omega GTMQSS T-type thermocouple located at the inlet of the wind tunnel.

The pitot tube is positioned 5.25-in above the wind tunnel floor, approximately 25.25-in upstream of the propeller, at the centerline of the tunnel. This positioning requires corrections to be applied to the velocity measurements to account for the propeller inflow at that pitot tube. This setup is used because traditional

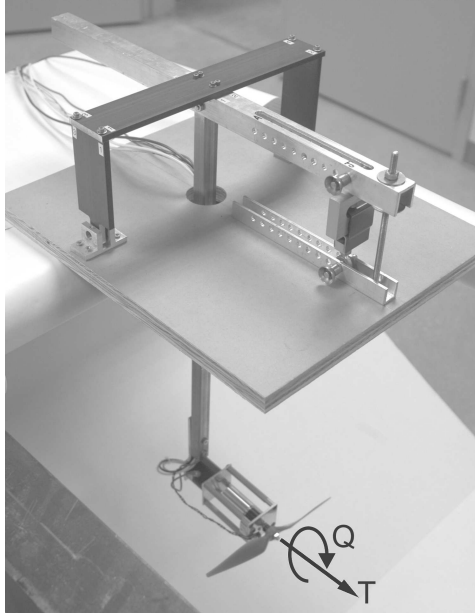


Figure 3. Test apparatus without fairing.

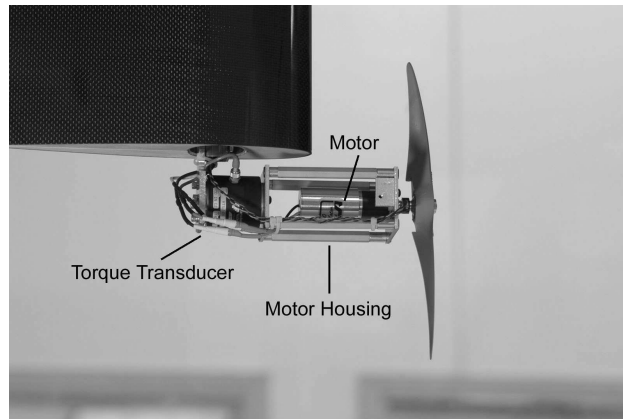


Figure 4. Torque transducer installed in the test rig.

techniques that use pressure measurements in the inlet to determine the velocity would be less accurate at the lower velocities tested.

E. Motor, Speed Controller and Propellers

The propellers were driven by the Astro 020 Planetary System (model 803P) made by AstroFlight. This motor and gearbox system used a 200-W motor with a 4.4:1 gear ratio that was capable of driving the propeller to a maximum speed of 7,500 RPM. For simplicity in the laboratory, a variable voltage switch mode power supply, made by BK Precision, is used to power the motor. The model used, the BK1692, can be set to an output voltage of 3 V to 15 V with a maximum current of 40 A.

Given that the Astro 020 is a brushless motor designed to work with a speed controller, a method was needed to send the appropriate signal to the speed controller. To set the rotational speed, a device called the ServoXciter EF, made by Vexa Control, was used. This device is designed to be used for testing R/C servos by allowing the operator to adjust the pulse-width of the signal being sent to the servo. Since the



Figure 5. APC Slow-Flyer, Sport, and Thin-Electric propellers.



Figure 6. Graupner CAM, CAM Slim, and Super-Nylon propellers.

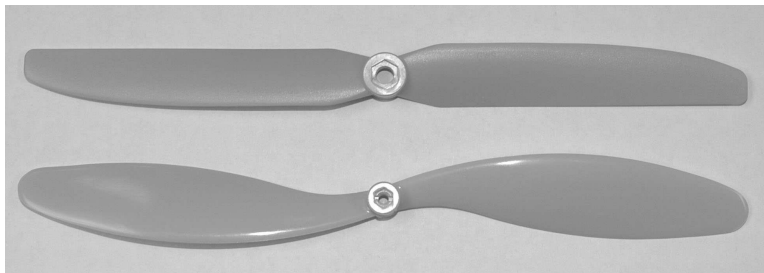


Figure 7. GWS Hyper-Drive, and Slow-Flyer propellers.

speed controller works with the same pulse-width modulation, the ServoXciter was used here as a throttle. Initially, the throttle was set manually using the knob on the ServoXciter. However, the device was modified so that it could be controlled with the data acquisition software, further automating the test. This was accomplished by modifying the ServoXciter to bypass the potentiometer, which was connected to the knob, and controlling the device with a command voltage from the data acquisition board.

The propellers that were tested span a variety of intended applications, including both gas and electric powered applications. Figures 5–9 show representative photographs of every style of propeller tested. All propellers were injection molded; no wooden propellers were tested.



Figure 8. Kyosho propeller.



Figure 9. Master Airscrew Electric, G/F, and Scimitar propellers.

F. Data Acquisition and Experimental Procedure

A brief summary of the data acquisition and experimental procedure⁵ is given here. All signals were acquired using a National Instruments NI PCI-6031E 16-bit analog-to-digital data acquisition board driven by custom software developed using LabVIEW[®], which is a C-based software suite from National Instruments, for creating Graphical User Interfaces (GUIs). The propeller speed measurement required a high data acquisition rate (20,000 Hz) to ensure that the signal from the photoreflector was accurately recorded. Due to limitations on the data acquisition board, this prohibited acquiring all of the data simultaneously. Thus, the propeller speed was first acquired at the higher data acquisition rate, then the remaining quantities (thrust, torque, dynamic pressure, atmospheric pressure, and temperature) were acquired simultaneously immediately thereafter at a reduced rate (1,000 Hz). This method proved to be appropriate, as the propeller speed measurements showed fluctuations below 0.1% over time periods significantly longer than those used for data acquisition.

The experimental procedure included setting up the experimental hardware and data acquisition system, calibration and calibration checks of the various instruments, and acquiring the performance data. The calibration checks performed during the setup process and the frequent calibrations performed throughout the tests ensured that the calibration data was as accurate as possible. Acquiring the performance data included obtaining the static performance data (where $V_\infty = 0$) as well as obtaining the remaining performance data in one of two test modes. The two possible test modes allowed the experimenter to sweep the advance ratio range by varying either the freestream velocity or propeller speed, while holding the other constant. In all the data reported here, the latter mode was used – the propeller speed was held constant while sweeping the tunnel speed in order to cover a range of advance ratios. The sweep in advanced ratio continued until the thrust became negative.

III. Data Reduction and Wind Tunnel Corrections

The data reduction process starts by converting the measured voltages into physical measurements of thrust, torque, rotational speed, dynamic pressure, atmospheric pressure, and temperature. The thrust, torque, dynamic pressure, air temperature, and atmospheric pressure are all found using the calibration data that is either provided by the transducer manufacturer or found in the calibration procedure, and the measured voltage. The signal obtained from the photoreflector is used to determine the rotational speed of the propeller. From these quantities, the propeller power, air density, and tunnel speed are calculated

according to

$$P = 2\pi nQ \quad (1)$$

$$\rho = \frac{P_{atm}}{R T_{air}} \quad (2)$$

$$V = \sqrt{\frac{2q}{\rho}} \quad (3)$$

Corrections are applied to the velocity to account for wind tunnel wall and blockage effects and to correct for the pitot tube being in an area influenced by the propeller inflow. These corrections are detailed below.

Finally, the above measured and derived quantities are non-dimensionalized to obtain the propeller performance data. The quantities include the thrust coefficient, power coefficient, and efficiency. For the static case ($J = 0$), the thrust and power coefficients are plotted against the propeller speed. For the non-static case ($J > 0$), the coefficients and the efficiency are plotted against the advance ratio. The definitions for the advance ratio, thrust and power coefficients, and propeller efficiency are given by

$$J = \frac{V}{nD} \quad (4)$$

$$C_T = \frac{T}{\rho n^2 D^4} \quad (5)$$

$$C_P = \frac{P}{\rho n^3 D^5} \quad (6)$$

$$\eta = J \frac{C_T}{C_P} \quad (7)$$

A. Propeller Speed Determination

Determining the propeller rotational speed from the photoreflector signal is a relatively straightforward process. First, the signal is analyzed to determine the minimum and maximum voltage readings. Next, the software analyzes each data point to determine if the reading is indicating a reflective or non-reflective surface. Each time the state changes, the switch is counted and the duration of the previous state is recorded. The propeller speed is then determined from the total number of revolutions and the sampling time used to acquire the signal.

B. Velocity Corrections

With the current setup, several factors are present that warrant velocity corrections, as the dynamic pressure measured is not equivalent to the true freestream dynamic pressure that would be found under normal, open-air operating conditions. The effect that the propeller inflow has on the velocity measurement is corrected with a scheme developed specifically for these tests. Two additional methods are used to account for the solid blockage caused by the fairing and the constriction of the propeller slipstream caused by the wind tunnel walls. The correction that accounts for the inflow caused by the propeller is iterative in nature, where the other two correction factors are not. Since the remaining two corrections are to be applied to the freestream velocity of the wind tunnel, the measured velocity is first corrected for the inflow. Subsequently, the remaining two corrections are applied to the corrected freestream velocity of the wind tunnel.

The correction to account for the inflow at the pitot tube models the induced flow with a double helical vortex extending “infinitely” downstream. The key factors in this correction include the radius and pitch of the helix, as well as the strength of the vortex. Below, Eqs. 10 and 12 show that the vortex strength is a function of the disk loading T/A . To develop this method, MATLAB[®] was used to set up the doubly infinite image system of helical vortices, as suggested in Ref. 11. This program was used to find the velocities induced both at the propeller disk and the pitot tube for varying helix pitch and radius using a unit strength vortex. Due to the computational effort required for this correction scheme, the method was not directly

incorporated into the data acquisition and reduction software. Accordingly, results from the MATLAB script are tabulated and the finite data sets are interpolated to find the velocity correction. Although this method is developed for a two-bladed propeller, it will suffice as a correction for a blade with an arbitrary number of blades. This results from the scheme being independent of the blade number (see below). For a propeller with a different number of blades, the two-blade equivalent vortex system corrects for the inflow. The iterative scheme is outlined below.

1. Set the freestream velocity. The first estimate uses the measured velocity and subsequent guesses use an under-relaxed estimate that combines the previous estimate and the corrected velocity according to Eq. 8, where $a = 0.5$.

$$\hat{V}_{\infty,+} = (1 - a) \hat{V}_{\infty,-} + a V_{corr} \quad (8)$$

where in the following

$$V_{\infty} = \hat{V}_{\infty,+} \quad (9)$$

2. Use Eq. 10, found in Ref. 12, to find the velocity induced at the propeller disk u_{disk} based on momentum theory.

$$u_{disk} = -V_{\infty} + \sqrt{V_{\infty}^2 + \frac{2T}{\rho A}} \quad (10)$$

3. Calculate the pitch of the vortex system based on the freestream velocity, induced velocity at the disk, and propeller tip speed using Eq. 11, as it is suggested in Ref. 11.

$$\tan k = \frac{V_{\infty} + u_{disk}}{V_{tip}} \quad (11)$$

4. Interpolate the data set for the inflow induced at the propeller disk using the propeller radius R and helix pitch k to find the inflow induced by a unit strength vortex $u_{\Gamma=1}$.
5. Calculate the vortex strength needed to produce u_{disk} using Eq. 12.

$$\Gamma = \frac{u_{disk}}{u_{\Gamma=1}} \quad (12)$$

6. Find the induced velocity at the pitot tube, \vec{V}_{pitot} , using the propeller radius, helix pitch k , and vortex strength Γ by interpolating the data set established for the inflow at the pitot tube.
7. Calculate the flow angle using Eq. 13, where the components of the velocity vector are those illustrated in Fig. 10.

$$\sin \Lambda = \frac{\sqrt{v_{pitot}^2 + w_{pitot}^2}}{V_{meas}} \quad (13)$$

8. Calculate the corrected freestream velocity using Eq. 14

$$V_{corr} = V_{meas} \cos \Lambda - u_{pitot} \quad (14)$$

Once the above scheme is used to correct the measured velocity for the inflow induced at the location of the pitot tube, the remaining two corrections are applied. The presence of the fairing in the wind tunnel reduces the cross-sectional area, increasing the velocity in the vicinity of the fairing. To correct for this, the 3-D solid blockage technique presented in Ref. 13 and shown in Eq. 15 is used. The factors K_1 and τ_1 (see Ref. 13) are determined from the fairing thickness ratio and the ratio between the model span and tunnel breadth, respectively. $\bar{V}_{fairing}$ and C are the volume of the fairing and the cross-sectional area of the wind tunnel, respectively.

$$\frac{\Delta V}{V_u} = \frac{K_1 \tau_1 \bar{V}_{fairing}}{C^{3/2}} \quad (15)$$

The boundary correction used to account for the wind tunnel walls was developed by Glauert in Ref. 14. The wind tunnel walls constrict the flowfield, causing an increased static pressure in propeller slipstream.

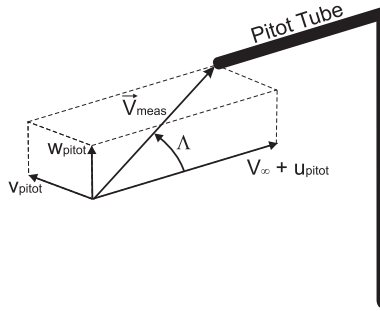


Figure 10. Measured velocity vector at the pitot tube.

Thus, the thrust that is developed would actually be produced by a lower freestream velocity in an unrestricted flow, which is based on a continuity analysis. The correction needed to account for this effect is presented in Eq. 16, where $\tau_4 = T/\rho AV_\infty^2$ and $\alpha_1 = A/C$.

$$\frac{V_{corr}}{V_\infty} = 1 - \frac{\tau_4 \alpha_1}{2\sqrt{1 + 2\tau_4}} \quad (16)$$

IV. Results

Although the propellers tested here are limited to non-folding, two-bladed propellers, a wide range of propeller styles were tested nonetheless. The majority of the propellers tested had diameters ranging from 9 in. to 11 in., though a few larger sizes were tested. For this series of tests, all of the propellers were tested without any alterations. Thus, any sharp and some times ragged leading edges that result from manufacturing processes remained. Some of the models tested are intended to be used on aircraft with electric motors, while others are designed to be used with fuel powered engines. With such a wide range of designs tested, a wide range of performance characteristics are observed. Here, the general trends found in the data are highlighted, although trends in the thrust and power coefficient are discussed briefly, the propeller efficiency is the main focus.

Looking at the entire set of data, one general trend is observed throughout (and will be illustrated in the figures to follow): as the propeller speed is increased, the performance improves. This result is most evident through increased efficiency. The degree of the improvement varies from propeller-to-propeller, but it is a trend that is consistent. This improvement is also seen in the thrust coefficient curves, as higher thrust coefficients are obtained with increasing propeller speed. The increased thrust is most easily seen looking at the static thrust plots.

The performance improvement that accompanies the increased propeller speed is an expected trend given that the propellers are operating with low chord-based Reynolds numbers and that increasing the propeller speed increases the Reynolds number. The work presented in Refs. 10 and 15–17, as well as myriad of other studies performed on low Reynolds aerodynamics, show that the aerodynamic performance of airfoils improves with increasing Reynolds numbers. Extending this improved performance to the airfoils on the propellers, shows that this trend is indeed expected. In the following, the trends observed for the different brands and styles are presented discussed.

A. APC Propellers

Three types of APC propellers were tested, namely the Slow Flyer, Sport, and Thin Electric propellers. Both the Slow Flyer and Thin Electric propellers are designed to be used solely with electric motors. The Sport propellers are designed to handle the increased torque produced by gas powered engines. The airfoil profiles on the Slow Flyer propellers are quite thin with a sharp leading edge, where the remaining two have thicker airfoil sections with rounded leading edges.

All of the APC propellers show some variation in the performance curves that is consistent with the overall trends. The Slow Flyers show the least variation in efficiency and the differences are larger near peak

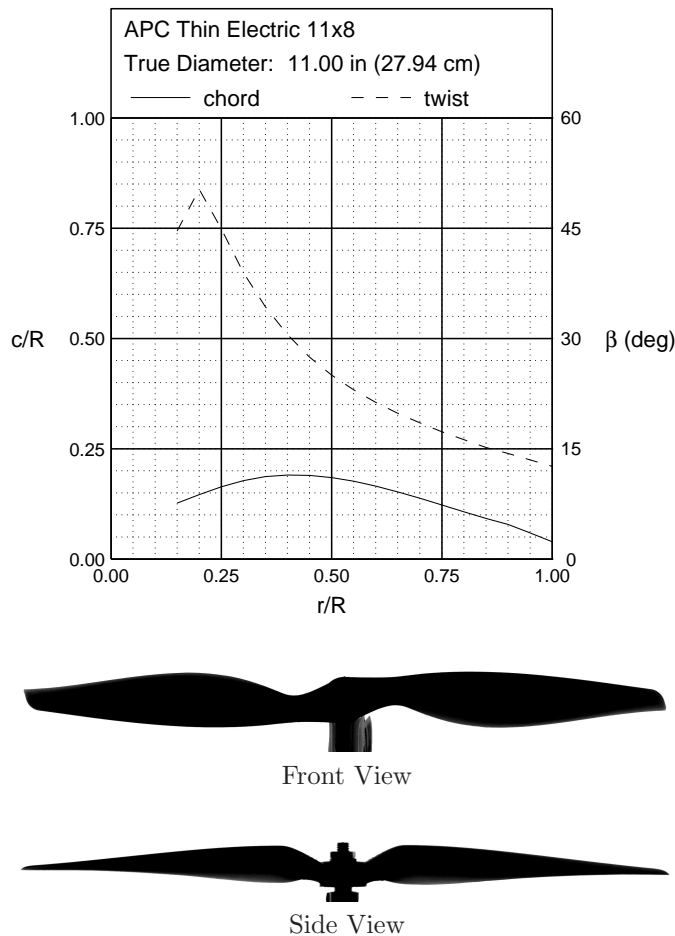


Figure 11. APC Thin Electric 11×8 geometric characteristics.

efficiency. The Sport propellers exhibit the largest efficiency variance that is observed over the entire range of advance ratio. Similar to the Slow Flyers, the Thin Electric propellers also show increased performance differences near peak efficiency.

One interesting trend is found in the thrust and power coefficients for the Thin Electric propellers; it is seen that variations in these coefficients are dramatically increased over a small range of advance ratio near the peak efficiency. The result is shown for the APC Thin Electric 11×8 propeller in Figs. 11–14.

B. Graupner Propellers

The four styles of Graupner propellers tested include the CAM, CAM Slim, Slim, and Super Nylon propellers. The former three are all designed specifically for use with electric motors, and the latter are intended to be used with gas powered engines. The CAM and Super Nylon propellers are designed with moderately thick airfoils with conventional round leading edges; where as, the CAM Slim and Slim propellers are designed with much thinner airfoil sections that have sharp leading edges.

The CAM propellers all show significant differences in the efficiency curves over the range of propeller speeds. These differences are rooted in significant variations in the thrust characteristics and minor variations in the power characteristics. Both the CAM Slim and Slim propellers show only minor variations in peak efficiency, with the Slim propeller showing some of the smallest variations in performance. The CAM Slim propellers show minor variations in both the thrust and power coefficients over a small range of advance ratio that correspond to the region of peak efficiency (see Figs. 15–18). Finally, the Super Nylons show moderate variations in the efficiency, with increased differences seen near the peaks.

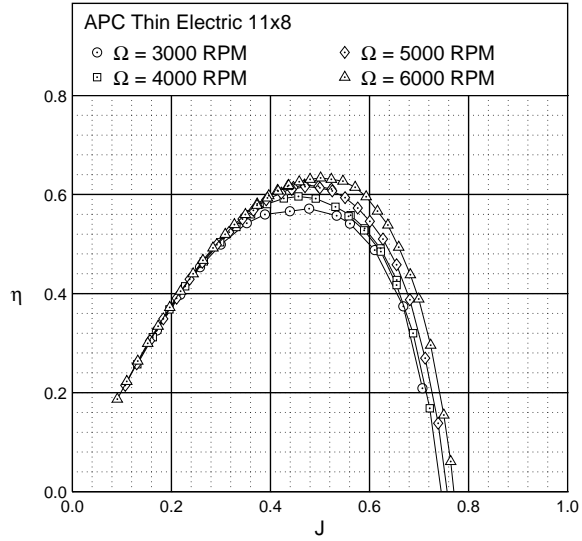


Figure 12. APC Thin Electric 11x8 efficiency curves.

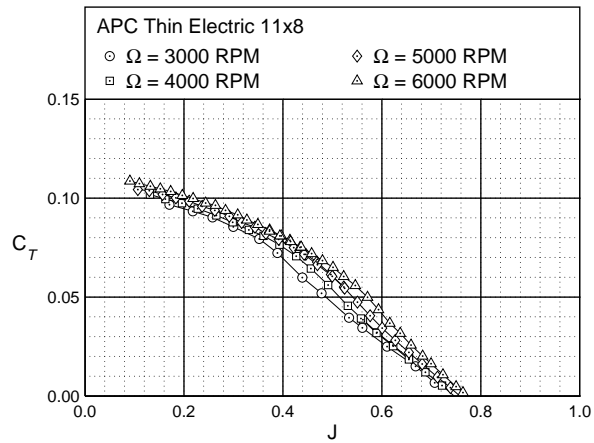


Figure 13. APC Thin Electric 11x8 thrust characteristics.

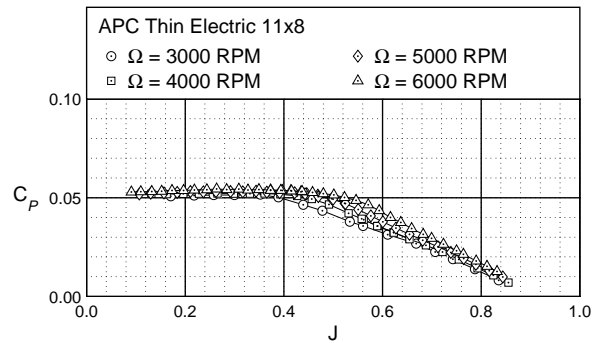
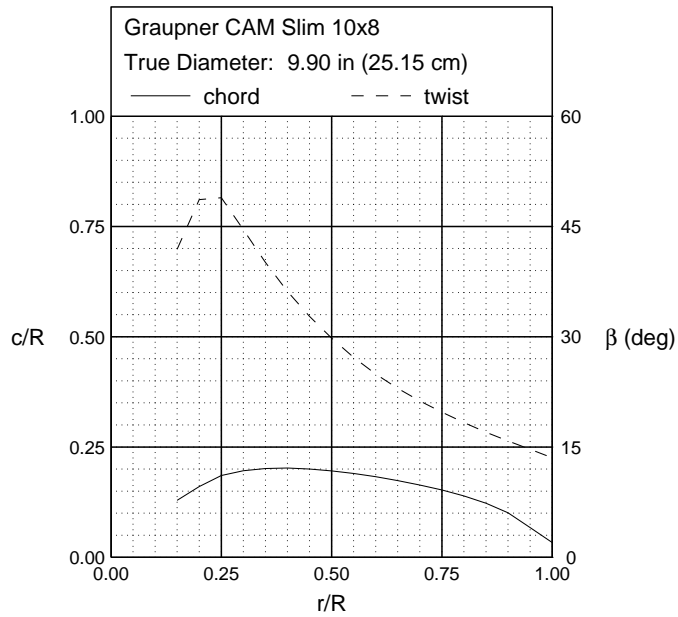


Figure 14. APC Thin Electric 11x8 power characteristics.



Front View



Side View

Figure 15. Graupner CAM Slim 10x8 geometric characteristics.

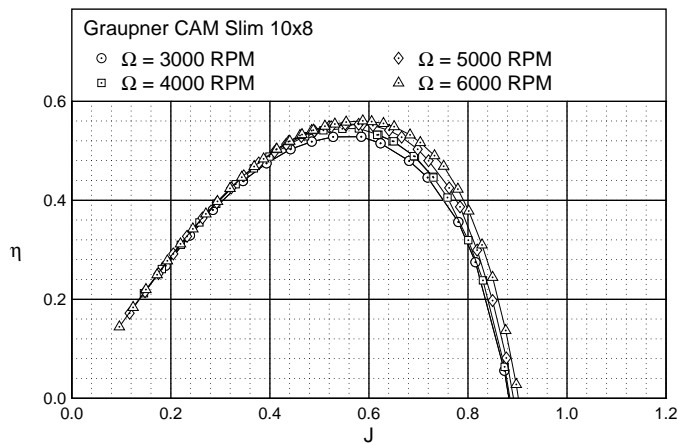


Figure 16. Graupner CAM Slim 10x8 efficiency curves.

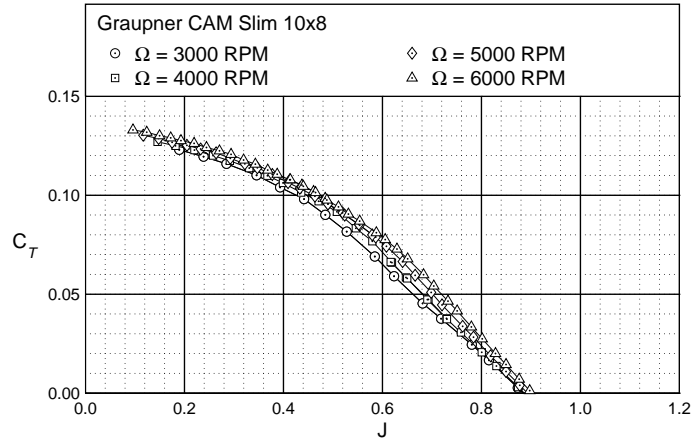


Figure 17. Graupner CAM Slim 10×8 thrust characteristics.

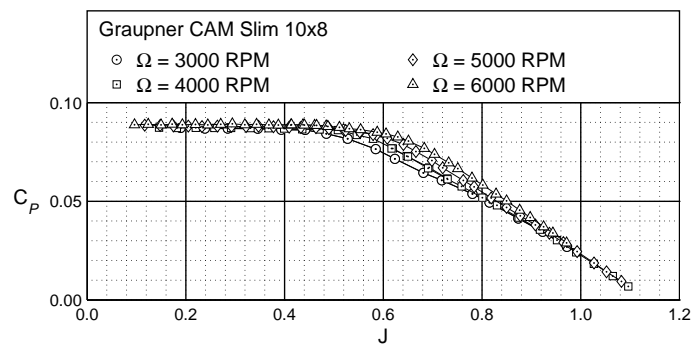


Figure 18. Graupner CAM Slim 10×8 power characteristics.

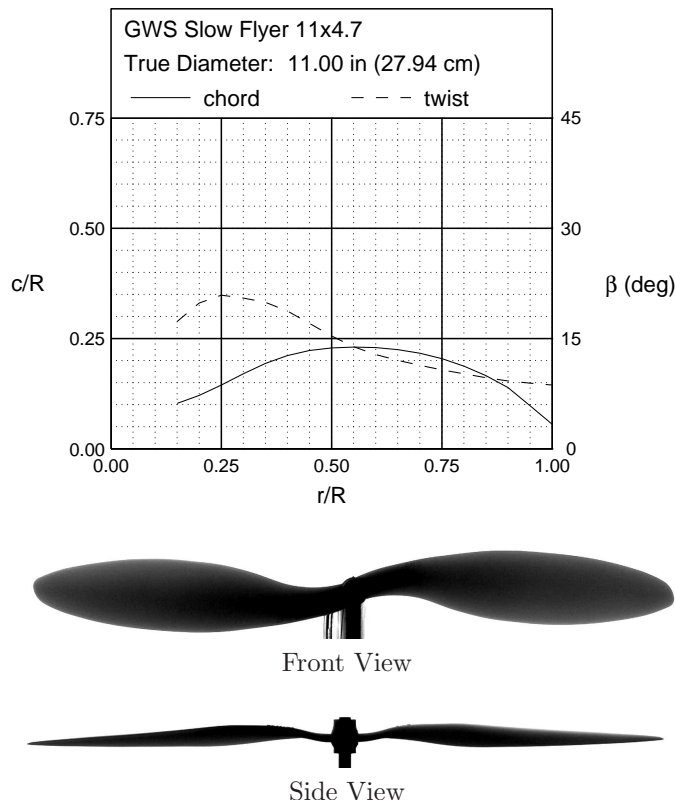


Figure 19. GWS Slow Flyer 11×4.7 geometric characteristics.

C. GWS Propellers

The two styles of GWS propellers that were tested are the Direct Drive and Slow Flyer propellers, both of which are designed to be used with electric motors. The Direct Drive propellers are designed to operate at higher rotational speeds, where the Slow Flyers are designed to operate at lower rotational speeds. Both styles of GWS propellers are designed with thin airfoils with sharp leading edges.

The GWS Direct Drive propellers show moderate variations in the peak efficiencies for the range of propeller speeds tested, where as shown in Figs. 19–22 the Slow Flyers show minimal variations in the performance. Looking at the GWS Slow Flyer data, unique trends are observed in both the efficiency and coefficient curves. In all other cases tested, increasing the propeller speed increased the efficiency, thrust coefficient, and power coefficient by varying degrees. However, it is observed here that the GWS Slow Flyers have lower efficiencies, thrust coefficients, and power coefficients at higher advance ratio. These trends are believed to be a result of blade flutter, as excessive noise was observed in a few extreme cases.

D. Master Airscrew Propellers

The Master Airscrew propellers tested included propellers limited to electric applications as well as propellers that could be used with either gas powered engines or electric motors. The Electric series propellers are designed to only be used with electric motors. Both the G/F and Scimitar series are designed for use with gas powered engines but can be easily used with electric motors as well. The Master Airscrew propellers are designed with relatively thick airfoils with round leading edges, but they have a sharp leading edge that is a result of the manufacturing process.

The Master Airscrew Electric series propellers show performance variations that are moderate in magnitude and consistent with the overall trends. The G/F series show some of the largest variations in both the efficiency and thrust coefficient curves, as the differences are exacerbated for the lower pitched propellers. The Master Airscrew G/F 11×4 shows that the peak efficiency nearly doubles over the range of propeller

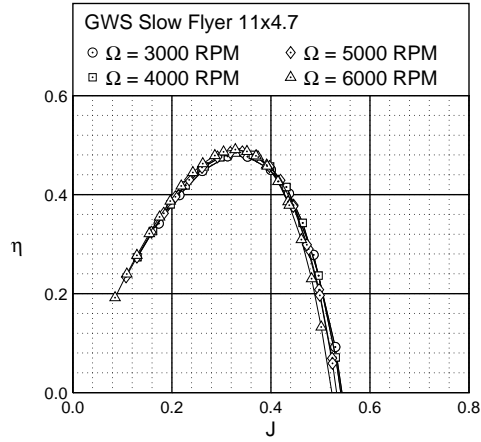


Figure 20. GWS Slow Flyer 11×4.7 efficiency curves.

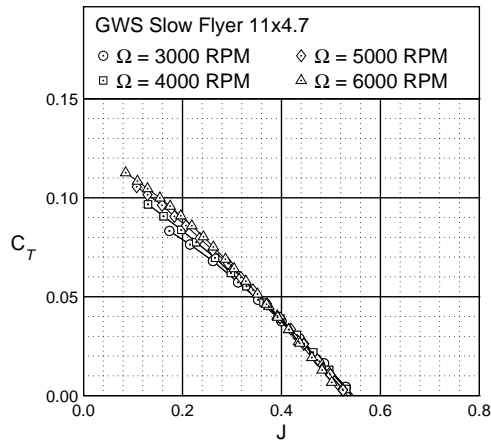


Figure 21. GWS Slow Flyer 11×4.7 thrust characteristics.

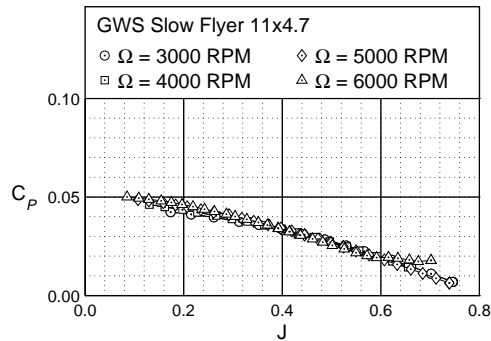


Figure 22. GWS Slow Flyer 11×4.7 power characteristics.

speeds tested (see Figs. 23–26). The Scimitar series shows moderate changes in performance for varying propeller speeds, where the differences are magnified over certain ranges of advance ratio.

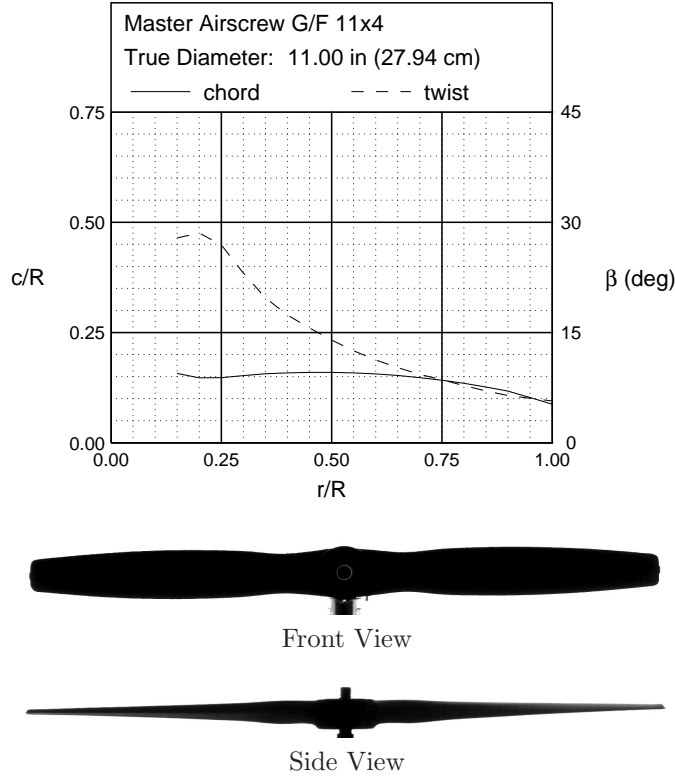


Figure 23. Master Airscrew G/F 11×4 geometric characteristics.

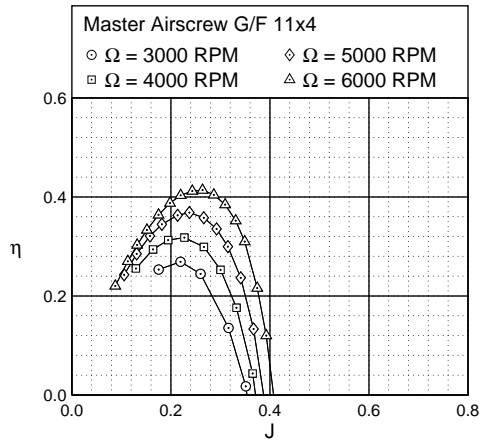


Figure 24. Master Airscrew G/F 11×4 efficiency curves.

V. Conclusion

In the research reported here, 79 propellers were tested and nearly all fit in the 9- to 11-in. diameter range. Thrust and torque were measured over a range of propeller advance ratios for discrete propeller speeds (RPM's) – typically four different values of RPM to examine low Reynolds number effects. Also static thrust was measured over a range of propeller speeds from nominally 1,500 to 7,500 RPM depending on the propeller diameter. The results showed significant Reynolds number effects with degradation in performance with lower RPM's. Also, over a range of propellers, the propeller efficiency varied greatly from

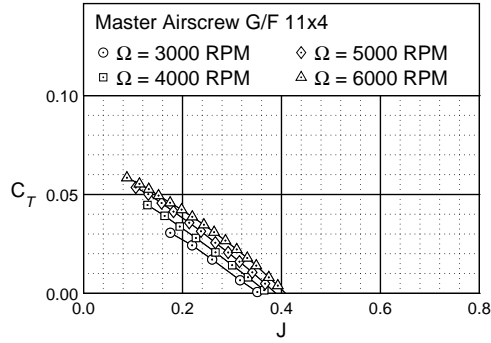


Figure 25. Master Airscrew G/F 11×4 thrust characteristics.

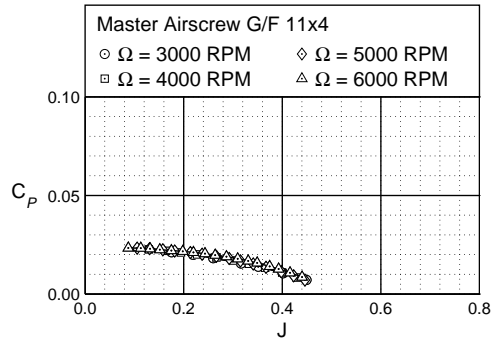


Figure 26. Master Airscrew G/F 11×4 power characteristics.

a peak near 0.65 down to near 0.28 for an exceptionally poor propeller. It is envisioned that the data gathered in these experiments will serve several purposes. The results will give aircraft designers a large database that can be used for selecting appropriate propellers for a wide variety of applications. Further, any beneficial or adverse trends found in the data will be used to improve design capabilities. Finally, prediction tools could be refined using the data gathered here.

Acknowledgments

The authors would like to thank Robert Deters, Paul Gush, and Kian Tehrani for their laboratory help in setting up and taking much of the propeller data report here and in the larger online collection. Also, the authors are grateful for the additional lab assistance provided by Keerti Bhamidipati, Chris Needham, Digesh Patel, and Sean Warrenburg.

References

- ¹Bailey, J. E., “Mini-RPV Engine-Propeller Wind Tunnel Tests,” *National Free Flight Society Annual Symposium Proceedings*, 1978.
- ²Durand, W. F., “Experimental Research on Air Propellers,” *NACA Report 141*, 1923.
- ³Bass, R. M., “Small Scale Wind Tunnel Testing of Model Propellers,” AIAA Paper 86-392, January 1986.
- ⁴Asson, K. M. and Dunn, P. F., “Compact Dynamometer System That Can Accurately Determine Propeller Performance,” *Journal of Aircraft*, Vol. 29, No. 1, 1992, pp. 8-9.
- ⁵Brandt, J. B., *Small-Scale Propeller Performance at Low Speeds*, Master’s thesis, Department of Aerospace Engineering, University of Illinois at Urbana-Champaign, Illinois, 2005.
- ⁶Merchant, M. P., *Propeller Performance Measurements for Low Reynolds Number Unmanned Aerial Vehicle Applications*, Master’s thesis, Department of Aerospace Engineering, Wichita State University, Kansas, 2005.
- ⁷Merchant, M. P. and Miller, L. S., “Propeller Performance Measurements for Low Reynolds Number UAV Applications,”

AIAA Paper 2006-1127, January 2006.

⁸Ol, M., Zeune, C., and Logan, M., “Analytical/Experimental Comparison for Small Electric Unmanned Air Vehicle Propellers,” AIAA Paper 2008-7345, August 2008.

⁹Brandt, J. B. and Selig, M. S., “Small-Scale Propeller Performance at Low Speeds – Online Database,” <http://www.ae.illinois.edu/m-selig/props/propDB.html>, 2010.

¹⁰Selig, M. S. and McGranhan, B. D., “Wind Tunnel Aerodynamic Tests of Six Airfoils for Use on Small Wind Turbines,” National Renewable Energy Laboratory, NREL/SR-500-35515, 2004.

¹¹Stepniewski, W. Z. and Keys, C. N., *Rotary-Wing Aerodynamics*, Dover Publications, New York, 1984.

¹²McCormick, B. W., *Aerodynamics, Aeronautics, and Flight Mechanics*, John Wiley & Sons, New York, 2nd ed., 1995.

¹³Barlow, J. B., Rae, W. H., Jr., and Pope, A., *Low-Speed Wind Tunnel Testing, Third Ed.*, John Wiley and Sons, New York, 1999.

¹⁴Glauert, H., *The Elements of Aerofoil and Airscrew Theory, Second Ed.*, University Press, Cambridge, 1948.

¹⁵Selig, M. S., Guglielmo, J. J., Broeren, A. P., and Giguère, P., *Summary of Low-Speed Airfoil Data, Vol. 1*, SoarTech Publications, Virginia Beach, Virginia, 1995.

¹⁶Selig, M. S., Lyon, C. A., Giguère, P., Ninham, C. N., and Guglielmo, J. J., *Summary of Low-Speed Airfoil Data, Vol. 2*, SoarTech Publications, Virginia Beach, Virginia, 1996.

¹⁷Lyon, C. A., Broeren, A. P., Giguère, P., Gopalarathnam, A., and Selig, M. S., *Summary of Low-Speed Airfoil Data, Vol. 3*, SoarTech Publications, Virginia Beach, Virginia, 1998.